Journal of The Electrochemical Society, **154** (5) A421-A426 (2007)
0013-4651/2007/154(5)/A421/6/$20.00 © The Electrochemical Society

A Two-Dimensional Model and Numerical Treatment for Mixed Conducting Thin Films

The Effect of Sheet Resistance

David S. Mebane,[a] Yingjie Liu,[b] and Meilin Liu[a,*,z]

[a]*School of Materials Science and Engineering and* [b]*School of Mathematics, Georgia Institute of Technology, Atlanta, Georgia 30332, USA*

A two-dimensional simulation was developed for thin-film, mixed ionic-electronic conductor (MIEC) electrodes. The equations for the steady-state (nonlinear) dc case are derived and solved through a finite volume discretization that enables a linear solver while preserving the nonlinear characteristics of the problem. Using parametric data for $La_{1-x}Sr_xMnO_{3\pm\delta}$ (LSM) collected from the literature, we found that the simulation is limited by electrochemically activated ionic transport at low cathodic overpotentials and co-limited by ionic and electronic resistance at high overpotentials. The current-voltage curves generated are similar in shape to most reported in the literature for thin LSM films. However, the simulation is much more resistive. While the cause for the discrepancy has yet to be validated, it seems clear that the sheet resistance of a thin-film electrode can critically influence its electrocatalytic behavior. This effect becomes more pronounced with the amplitude of polarization and the decrease in dimension, implying that it can be significant in patterned or nanostructured electrodes.
 [DOI: 10.1149/1.2710204]

Manuscript submitted August 24, 2006; revised manuscript received December 28, 2006. Available electronically March 14, 2007.

Thin films and patterned electrodes are effective vehicles for study of electrodics in mixed ionic-electronic conductors (MIECs), because it is possible to precisely control the geometry related to the triple phase boundary (TPB) and bulk reaction pathways. Many experimental studies involving thin films and patterned electrodes for the electrode MIECs $La_{1-x}Sr_xMnO_{3\pm\delta}$ (LSM) and $La_xSr_{1-x}Co_{1-y}Fe_yO_{3-\delta}$ (LSCF) have appeared over the years.[1-20]

Modeling studies on MIECs to date have avoided consideration of sheet resistance, by assuming either perfect current collection (an implicit assumption in any one-dimensional model)[21-23] or uniform Fermi level throughout the material.[24-31] Such assumptions are usually valid for a macroscale electrode, as electronic conductivities far outstrip their ionic counterparts in the most popular MIECs for electrode applications. However, recent studies on $La_{0.8}Sr_{0.2}MnO_{3\pm\delta}$ (LSM20) patterned electrodes found evidence of a sheet resistance effect, which calls these assumptions into question for the case of high aspect ratio.[2,13] These results force a reconsideration of the effects of sheet resistance if patterned electrodes and thin films are to be more widely used for scientific inquiry, and if nanostructured electrodes are to be considered for high performance applications.[32-34]

A rigorously derived model explicitly treating the effects of both ionic and electronic transport in thin-film MIECs has been developed. The simulation treats the case of steady-state dc polarization in the linear or nonlinear response regime on a two-dimensional domain. The application of nonlinear numerical schemes for the treatment of multiple species in one dimension is a relatively well-studied problem.[21,35] However, the multidimensional case can present difficulties for numerical analysis, especially with mixed boundary conditions.

Using parameter data collected from the literature, the simulation shows that sheet resistance will play an important role for thin LSM films contacted by moderate-sized Pt mesh at moderate to high overpotentials, but not in the limit approaching zero polarization. The shape of the model-generated current-voltage (I-V) curves, which conform to most found in the literature for LSM thin films, are dissected in terms of rate-limiting steps, which are bulk ionic transport and sheet resistance for our parameterization. However, when compared to the experimental results, we found that the electrode resistance generated by the model in the low-polarization limit was considerably higher. Possible reasons for this divergence are discussed.

* Electrochemical Society Active Member.
z E-mail: meilin.liu@mse.gatech.edu

Experimental

Model.— Figure 1 depicts the model geometry in schematic form. Figure 1a shows the top view, and Fig. 1b the cross-sectional view. Neglecting cell edge effects, we can reduce the domain to the two-dimensional (2D) region enclosed by the dashed-line box in Fig. 1b, which represents the smallest symmetrical element in the cross section.

For simplicity, the model assumes a two-step reaction sequence at the air-exposed surface. In the Kröger-Vink notation, that sequence is

$$\frac{1}{2}\,O_2 + s \rightarrow O'_{ads} + h^{\cdot} \qquad [1]$$

$$O'_{ads} + V_{\ddot{O}} \rightarrow O^{x}_{O} + h^{\cdot} + s \qquad [2]$$

where $V_{\ddot{O}}$ is an oxygen vacancy, O'_{ads} is an adsorbed oxygen, $h^{\cdot}$ is an electron hole, and s is an empty adsorption site on the surface of

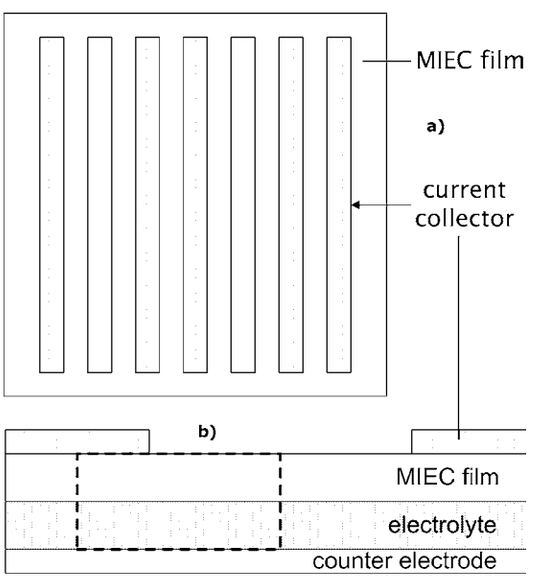

Figure 1. (a) Top view and (b) cross-sectional view of the cell geometry. The dashed-line box in (b) indicates the smallest symmetrical element in the cross section, which is used as the model geometry.

the MIEC. Taking the surface polarization into account, the rate equations for these reactions are[36,37]

$$r_{ads} = k^0_{ads}\left[\frac{(1-\theta)}{(1-\theta_0)}\exp\left(\frac{-\alpha_3 F\Delta\chi_s}{RT}\right) - \frac{\theta c_h}{\theta_0 c_{h,0}}\exp\left(\frac{(1-\alpha_3)F\Delta\chi_s}{RT}\right)\right] \quad [3]$$

and

$$r_{inc} = k^0_{inc}\left[\frac{\theta c_v}{\theta_0 c_v}\exp\left(\frac{\alpha_4 F\Delta\chi_s}{RT}\right) - \frac{(1-\theta)c_h}{(1-\theta_0)c_{h,0}}\exp\left(\frac{-(1-\alpha_4)F\Delta\chi_s}{RT}\right)\right] \quad [4]$$

where c_v and c_h are the concentrations of oxygen vacancies and holes, respectively, taken at the MIEC surface, the k^0 terms are exchange rate constants, θ is the site fraction of adsorbates, the α terms are transfer coefficients, and $\Delta\chi_s$ is the difference between the electrostatic potential drop across the surface and its equilibrium value. The subscript 0 denotes the equilibrium value.

The flux of species k in the MIEC and electrolyte is

$$N_k = -u_k c_k \nabla\mu_k \quad [5]$$

where u_k is the mobility, c_k the concentration, and μ_k the electrochemical potential of species k. If we adhere to a strictly dilute model, which should usually be valid for mobile species in LSM, we can rewrite the above flux in terms of the concentration and the electrostatic potential[38]

$$N_k = -RTu_k\nabla c_k - z_k F u_k c_k \nabla\phi \quad [6]$$

where z_k is the formal charge on species k, and ϕ is the electrostatic potential. If we assume that only vacancies and holes are mobile, with the (negatively charged) cation defects essentially immobile, then the values for k are v and h in the MIEC and v only in the electrolyte.

The mass continuity equation is

$$\frac{\partial c_k}{\partial t} = -\nabla\cdot N_k + G_k \quad [7]$$

where G_k is the net generation rate of species k, which is zero for all species in the bulk phases. The principle of electroneutrality is a very good approximation in the bulk phases, and we employ it even though it prevents a detailed description of the interfaces

$$F\sum_k z_k c_k + \rho_b = 0 \quad [8]$$

where ρ_b denotes the background charge. Combining Eq. 5, 7, and 8 in the MIEC produces a coupled system of equations in c_v and ϕ. In the electrolyte, electroneutrality leads to a constant $c_{v,e} = c_{v,e0}$, where the subscript e denotes the electrolyte, and the equation of state becomes Laplace's equation.

The boundary conditions are the potential applied across the current collector and the counter electrode, which are considered to be reversible interfaces, with a grounded counter and no loss in the external circuit. A zero-flux condition holds at symmetrical boundaries, and Eq. 3 and 4 define the flux of vacancies at the air-exposed surface. In addition to the air-surface reactions, the vacancy transfer from the electrolyte to the MIEC is an electrochemical reaction, whose rate obeys[36]

$$r_v = k^0_v\left[\exp\left(\frac{2\alpha_9 F\Delta\chi_i}{RT}\right) - \frac{c_v}{c_{v,0}}\exp\left(-\frac{2(1-\alpha_9)F\Delta\chi_i}{RT}\right)\right] \quad [9]$$

where the value of c_v is taken at the interface. Assuming zero interfacial polarization at equilibrium, the $\Delta\chi_i$ term in Eq. 9 is the jump in electrostatic potential across the electrolyte/MIEC interface.

Discretization.— We derived a conservative, finite volume discretization that is second-order in space and first-order in time.

Table I. Parameter values for LSM20.

Parameter	Value	Units
$c_{v,0}$	3.0×10^{-5}	mol/m^3
$c_{h,0}$	1.1×10^{4}	mol/m^3
k^0_{inc}	6.7×10^{-7}	mol/m^2 s
u_v	2.6×10^{-14}	mol m^2/J s
u_h	1.4×10^{-12}	mol m^2/J s
$c_{v,e0}$	5.0×10^{2}	mol/m^3
$u_{v,e}$	5.8×10^{-14}	mol m^2/J s

Keeping time dependence in the solver (the solution effectively iterates to steady-state) enables its linearization through mixing of implicit and explicit terms.

Defining the MIEC domain by a set of rectangular control volumes $\{P_{ij}\}$, we integrate Eq. 7 over the cell area located at (x_i, y_j). This yields the standard form for a semidiscrete finite volume scheme

$$\frac{\partial\hat{c}_{i,j}}{\partial t} = -\frac{1}{\Delta x}(\hat{N}_{i+1/2} - \hat{N}_{i-1/2}) - \frac{1}{\Delta y}(\hat{N}_{j+1/2} - \hat{N}_{j-1/2}) \quad [10]$$

where the carat indicates averages over the cell area (for $\hat{c}$) and cell boundary ($\hat{N}$). We then apply the backward Euler time discretization

$$\hat{c}^{n+1}_{i,j} - \hat{c}^n_{i,j} = -\frac{\Delta t}{\Delta x}(\hat{N}^{n+1}_{i+1/2} - \hat{N}^{n+1}_{i-1/2}) - \frac{\Delta t}{\Delta y}(\hat{N}^{n+1}_{j+1/2} - \hat{N}^{n+1}_{j-1/2}) + \mathcal{O}(\Delta t) \quad [11]$$

where the superscript n refers to the value at time t_n. We approximate N at a cell boundary based on the field values in neighboring cells

$$\hat{N}^{n+1}_{i+1/2} = -\frac{RTu}{\Delta x}(\hat{c}^{n+1}_{i+1,j} - \hat{c}^{n+1}_{i,j}) - \frac{zFu(\hat{c}^n_{i,j} + \hat{c}^n_{i+1,j})}{2\Delta x}(\hat{\phi}^{n+1}_{i+1,j} - \hat{\phi}^{n+1}_{i,j}) + \mathcal{O}(\Delta x^2) \quad [12]$$

The restriction of the concentrations in the drift term to the nth time level allows for a linear solver, which greatly increases the available options. Because the MIEC equations cannot be decoupled, we solved them successively, using the equation written for vacancy conservation to solve for vacancy flux while keeping electrostatic potential constant, then using the hole conservation equation to solve for electrostatic potential while keeping vacancy concentration constant, repeating the process until steady-state is reached. We used a line-by-line iterative solver for each step.[39]

For the parameters listed in Table I, a geometry of 400 μm in the breadth of current collector and 400 μm between current collectors, film heights from 50–1000 nm, and at moderate cathodic overpotentials (down to −750 mV), the scheme stabilized with respect to the mesh at a cell count of 60 in the MIEC y-direction (the thin dimension of the film) and 100 in the x-direction. The scheme stabilized with respect to the time step at $\Delta t = 10^{-5}$. The iterations to each time step terminated when the change in the infinity-norm of the vacancy vector (equal to its largest element) from that of the previous iteration was less than 0.1%. The simulation stopped when the current of vacancies at the electrolyte interface matched that of vacancies and holes at the air surface to within 0.01%. Convergence was fast, usually a matter of a few seconds, although this could extend to several minutes depending on overpotential, film thickness and the specific parameters.[c]

[c] The authors invite questions on the numerical scheme and are willing to provide C-language code and/or compiled executables for both Windows and Unix platforms.

Parameters.— We require reliable data for a number of physical parameters. We sought data for LSM20 and 8% Y_2O_3-doped ZrO_2 at an operating temperature of 750°C in air. We obtained estimates for all required parameters except k_v^0.

The equilibrium concentration of oxygen vacancies in LSM20 at atmospheric p_{O_2} cannot be directly measured, and must therefore be calculated using classical defect models derived from nonstoichiometry data[40-44] or thermodynamic models derived from phase equilibria.[45] Because it is broad in its consideration of defect phenomena yet straightforward in presentation, we used the classical defect model developed by Poulsen.[44] Poulsen's model requires three equilibrium constants, estimated from nonstoichiometry data. We obtained these constants from Nowotny and Rekas ("random defect model").[42] Note that Nowotny and Rekas's method of calculating equilibrium constants from nonstoichiometry data seems somewhat inexact, as gravimetry-derived deviations from stoichiometry are used interchangably with vacancy concentration in their calculations, apparently without regard to the influence of cation vacancies. However, Nowotny and Rekas's listing of standard enthalpies and entropies is convenient for conversion of the data to different temperatures, and the constants thus calculated are easily converted to the form required by Poulsen's model. Calculating the values of equilibrium constants at 750°C for the Schottky reaction, reduction of LSM and disproportionation of Mn from Nowotny and Rekas's data, and employing Poulsen's technique for the small polaron model in Matlab code (with A-site nonstoichiometry assumed to be 5%), yielded the values for $c_{v,0}$ and $c_{h,0}$ reported in Table I.

Kilner noted a correlation between the diffusivity of oxygen tracer atoms and the effective surface exchange constants in MIECs used for SOFC cathodes.[46] This correspondence suggests that the reactions at the air-exposed surface in these MIECs are rate limited by some step involving oxygen vacancies at the surface (although the exact nature of this step is not yet known). In our surface model (Eq. 1 and 2), the only reaction involving oxygen vacancies is the incorporation step Eq. 2. We therefore assume that the incorporation step is rate-limiting, and Reaction 1 is in equilibrium.

This assumption carries several implications. First, it is no longer important to find an accurate value for k_{ads}^0, it must simply be considerably higher than k_{inc}^0. Second, an equilibrated adsorption step, combined with the fact that in the case of LSM the concentration of holes is always much larger than that of vacancies, means that the concentration of adsorbates on the surface will not deviate appreciably from equilibrium. Because the deviation of the adsorbate concentration from equilibrium controls the surface potential, $\Delta\chi_s \approx 0$. Third, the value for the equilibrium site fraction, θ_0, is not important.

The final implication of incorporation rate control at the surface is that the average exchange constant measured via isotope exchange/secondary-ion mass spectroscopy (SIMS) and the exchange rate constant k_{inc}^0 of our model are the same. With that in mind, we used DeSouza and Kilner's measurement of the oxygen exchange rate constant.[47] We also used DeSouza's isotope exchange/SIMS measurement of the oxygen tracer diffusivity and activation energy in LSM20, which along with the formula $D^* = f^* D_v[V_{\ddot{O}}]$, where D^* is the tracer diffusion coefficient and f^* is the tracer correlation factor (equal to 0.69), yields the diffusivity of vacancies.[48] The mobility then follows directly from the Nernst-Einstein relation. These values are reported in Table I.

Because of its high electronic transference number, the electronic conductivity of LSM20 can be accurately measured. The electronic conductivity at 750°C was calculated from conductivity and activation energy data reported in Minh and Takahashi,[49] and the mobility of electron holes follows from the conductivity. The oxygen vacancy concentration in the electrolyte was calculated by assuming a full ionization of acceptor dopants (Y'_{Zr}) and 100% compensation by oxygen vacancies. Ionic conductivity data[49] was then converted into the value for $u_{v,e}$ appearing in Table I.

We assumed that the transfer coefficient in Eq. 9 is 1/2.

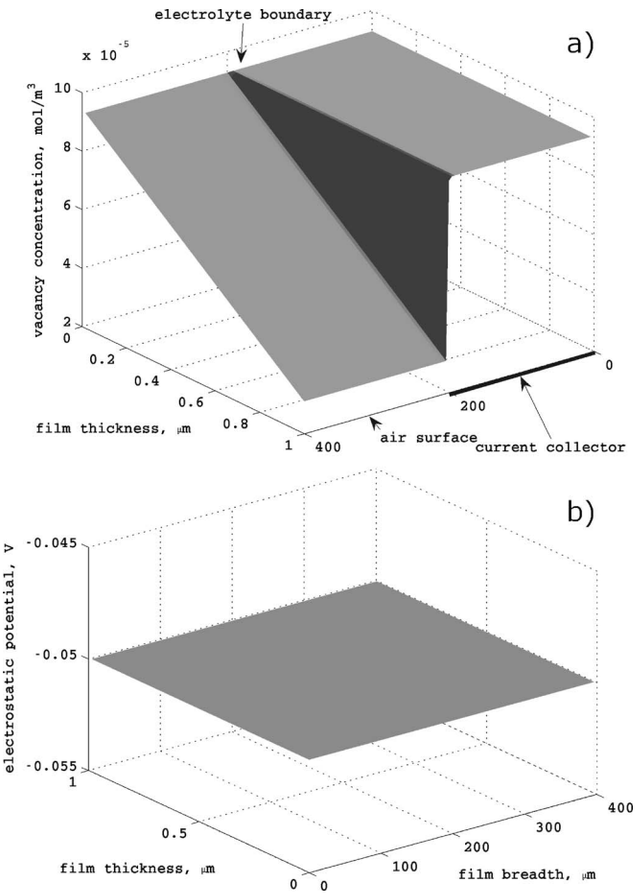

Figure 2. (a) Vacancy and (b) electrostatic potential distribution for a 1 μm thin film with a 400 μm wide current collector and 400 μm between current collectors, at −50 mV, using the parameters of Table I.

As mentioned, the only parameter whose estimate eluded us is the exchange rate constant at the LSM-YSZ interface, k_v^0. Our literature search revealed no attempts at direct measurement of this parameter, but a parametric study by Baumann et al. indicated that the vacancy transfer reaction between LSCF and the electrolyte is not rate limiting.[1] We assume this is the case for LSM-YSZ.

Results and Discussion

Sheet resistance at high cathodic overpotential.— Figure 2 shows a typical result for the simulation, using the parameters listed in Table I and a cell geometry of 400 μm in current collector width, 400 μm between current collectors, and 1 μm in film height, with a cell overpotential of −50 mV. Here we see the basic response for the vacancy distribution (part a) and the potential (part b) in the MIEC film. There is almost zero sheet resistance at this geometry and polarization, as reflected by the nearly equipotential state of the MIEC. The vacancy gradient drives species from the region under the current collector toward the air surface, and from the interface with the electrolyte toward the top surface. The gradient in holes runs in the opposite direction, as dictated by the electroneutrality condition. The flux of holes is not simply opposite to that of vacancies, however; due to their much higher concentration the drift of holes due to the tiny gradients in electrostatic potential counteract the concentration gradient, driving holes toward the current collector.

Figure 3 shows the situation at −750 mV. There is now a significant sheet resistance effect, with the electrostatic potential rising almost 150 mV at the midpoint between current collectors (Fig. 3b)

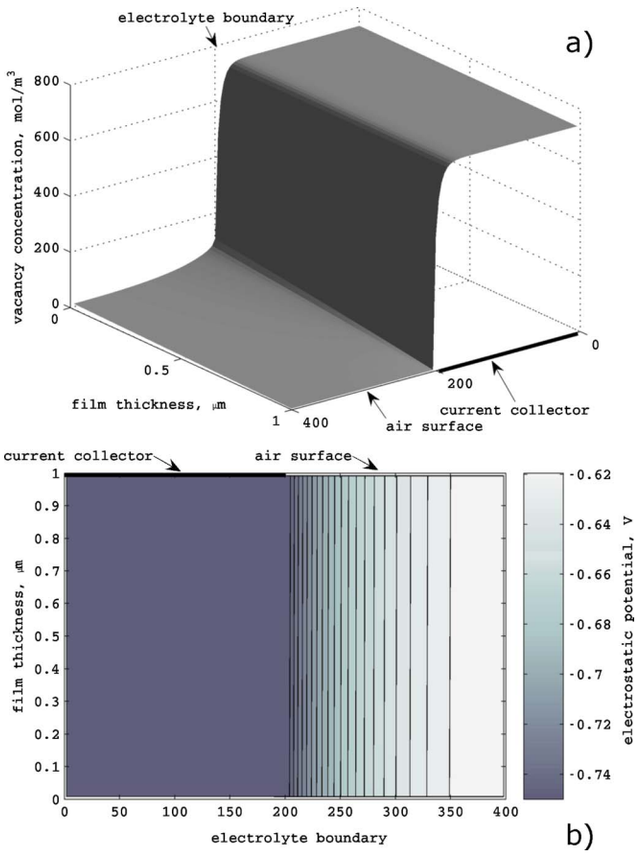

Figure 3. (Color online) (a) Vacancy and (b) electrostatic potential (contour plot) for the same film geometry and model parameters as Fig. 2, at −750 mV polarization.

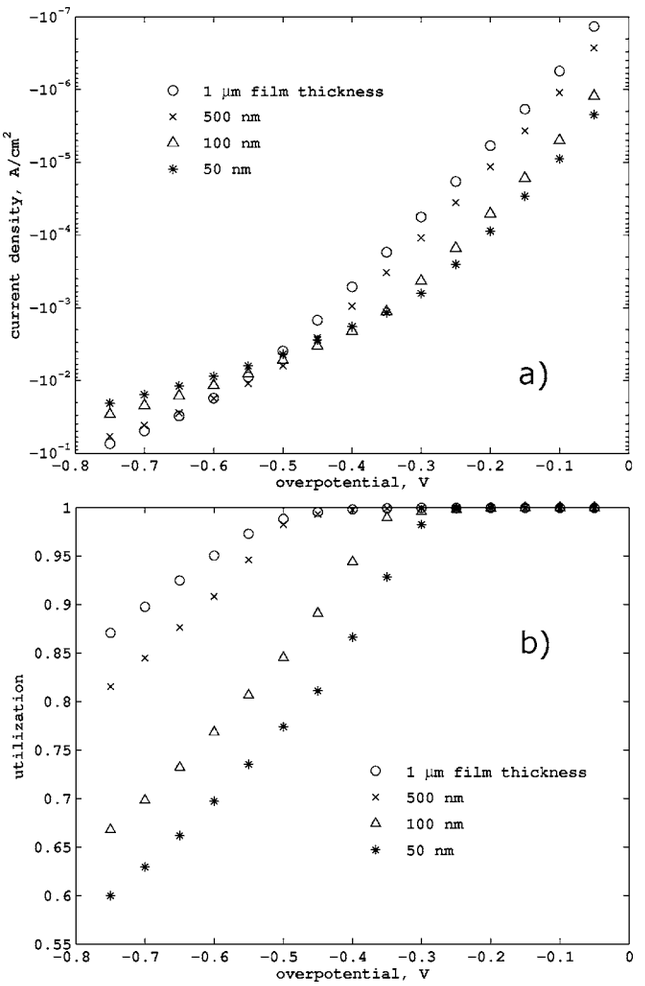

Figure 4. (a) I-V curves and (b) utilization curves for films of various thicknesses.

and the vacancy distribution shows a strong variation, with a precipitous drop occurring at the current collector edge (Fig. 3a). It is clear that the gradient in vacancies and potential right at the junction is nearly singular, and this is a source of instability at even higher cathodic overpotentials.[d] The maximum vacancy concentration underneath the current collector is 736 mol/m^3, which translates to a vacancy site fraction of about 0.028. This is over seven orders of magnitude higher than at equilibrium.

Figure 4 shows a set of I-V curves for films of various thicknesses, from 50 nm up to 1 μm (Fig. 4a) and the corresponding utilization curves (Fig. 4b). Here we define "utilization" as the percentage of the potential applied at the current collector attained by the average electrostatic potential in the portion of the MIEC underneath the air-exposed surface. The semi-log I-V plot (part a) shows two straight-line regions, with the slope at high overpotentials shallower than that at low overpotentials. Comparing the two parts of Fig. 4 reveals that the change in slope is due to a transition to a sheet resistance-limited regime.

Transport limited at low cathodic overpotential.— The straight lines in the semi-log plots suggest a process limited by charge transfer. However, we chose the value of k_v^0 in Table I specifically because we did not want a limiting charge transfer process, and all of the evidence suggests that we succeeded (at least at low overpotentials). Figure 5 shows a set of I-V curves taken at 1 μm thickness with vastly different values for k_v^0 but with other parameters held to their Table I values, with very little change in the film resistance above −500 mV. However, the change in current with the mobility of vacancies (Fig. 6) is much more pronounced; the correspondence

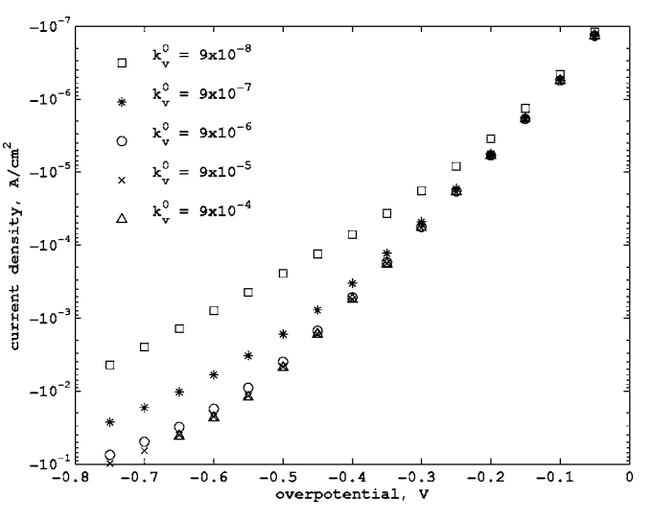

Figure 5. I-V curves for a 1 μm film and various values for the constant k_v^0.

[d] Possible cures for this instability are an upwind formulation in the drift term of the flux or a compact scheme. For the purposes of the present analysis, the stability of the current scheme is sufficient.

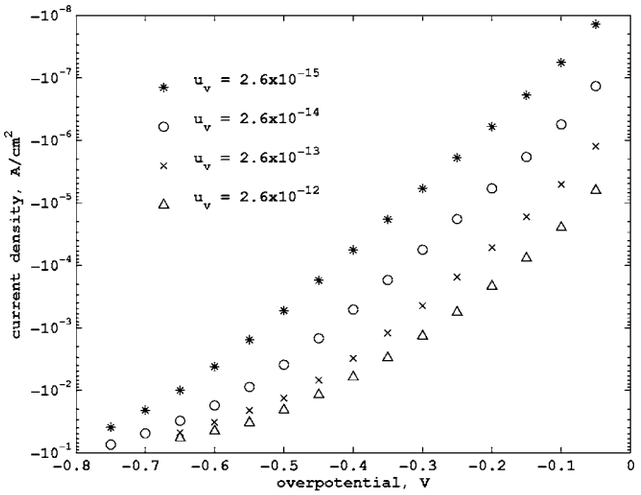

Figure 6. I-V curves for a 1 μm film and various values for the mobility of vacancies, u_v.

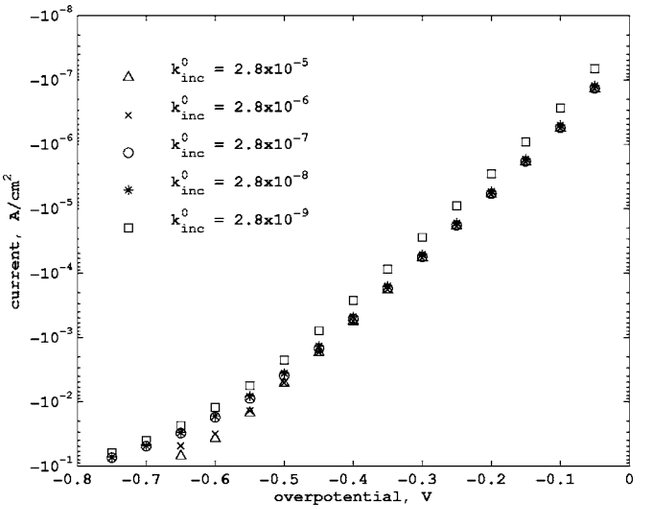

Figure 8. I-V curves for a 1 μm film and various values for the incorporation rate constant, k^0_{inc}.

is almost 1:1. Figure 7 is a log-log plot showing the almost precisely inverse relationship between thickness and current at −5 mV. Actually, the slope is slightly greater than 1, which is likely due to the increasing reduction of the bulk as thicknesses decrease. As cathodic overpotentials increase, the slope of the log-log current-thickness plot also decreases, eventually becoming negative.

Figure 8 shows that in this parameterization, k^0_{inc} is right at the edge of colimitation with the bulk, as changes of increasing magnitude are seen for a reduction in the parameter but there is virtually no change for increases.

These features, exponential I-V relationship with linear relationship between thickness and resistance, reflect those seen in thin-film experiments and in dc models of mixed conducting cathodes. Our explanation for the behavior is essentially the same as that of Svensson.[26] To say it succinctly, Boltzmann statistics yields an exponential relationship between the extra energy applied to the system and the excess concentration of vacancies which the MIEC may accomodate, in analogy to Hebb-Wagner polarization.[50] However, in our treatment there is no need to break down the overall applied voltage into separate terms as is normally done,[25,26,29] because everything is tied up in the single kinetic expression of Eq. 9.

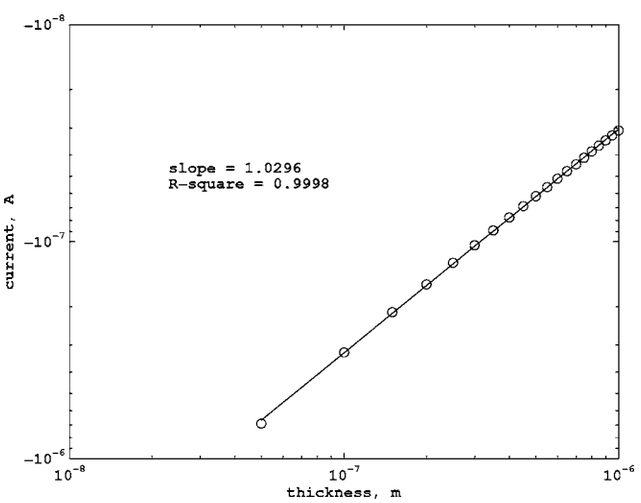

Figure 7. Log-log plot of thickness vs current for films at −5 mV overpotential.

When sheet resistance becomes significant at high overpotentials, the effect is to limit the active area of the film. However, if ionic transport near the current collector is still rate-limiting, current will still respond exponentially to overpotential increases. Therefore the response is another straight-line region in the semi-log plot, albeit with a shallower slope.

Comparison with experimental studies.— Because we chose our parameters from the literature based on LSM, we now briefly survey studies featuring LSM thin films. Mizusaki[15] and Ioroi[8,9] reported on thin LSM films deposited by laser ablation (for Mizusaki) and EVD (for Ioroi). The most striking feature of the comparison between these experiments and the model is the large disagreement on area-specific polarization resistance (ASR) near the limit of zero polarization. Ioroi reports open-circuit ASR on the order of 250 Ω cm^2 for 1.7 μm thick $LaMnO_3$ at 800°C in air,[8] and Mizusaki reports the same order of magnitude (somewhat lower) for an 0.9 μm $La_{0.63}Sr_{0.27}MnO_{3\pm\delta}$ film at 800°C. By contrast, the model's ASR for 1 μm thick LSM20 at −5 mV (reflecting 750°C in air) is 6.5 × 10^5 Ω cm^2, a difference of over three orders of magnitude.

While several factors may explain the discrepancy, one likely cause is that the experimental films are defective in some unaccounted-for manner. We base this conclusion on more recent results from Imanishi et al.[7] Imanishi and co-workers developed a method for producing epitaxial films of LSC and LSM on YSZ substrates (see also Mori et al.[16]). Epitaxial or near-epitaxial films are much less likely to contain nanoporosity, and by definition contain fewer grain boundaries. The dc-measured, electrolyte compensated current for Imanishi's 30 nm LSM20 film deposited on the YSZ (110) surface at approximately −17 mV, 0.1 atm p_{O_2}, and 700°C was −10^{-5} A cm^{-2}, whereas that of our model at the same thickness and polarization at 750°C is −7.4 × 10^{-7} A cm^{-2}, still over an order of magnitude lower, but notably, much closer than the earlier experiments. At higher overpotentials, the difference narrows even more: Imanishi reports −10^{-4} A cm^{-2} at approximately −109 mV, whereas the simulation gives −1.6 × 10^{-5} A cm^{-2}.

Qualitatively, the shape of Imanishi's I-V curves are consistent with the shape of the curves in Fig. 4, displaying two plausibly linear regimes on the semilog scale separated by a transition region. I-V curves reported by Mizusaki and Endo[6] display similar shapes.

The remaining difference in ASR between Imanishi and the model is probably due (in large part) to incorrect values for diffusivity, equilibrium vacancy concentration, incorporation rate constant or a combination. It seems otherwise unlikely that the model's

approximations (at low overpotential, these chiefly pertain to the surface model) would make an order of magnitude difference. The narrowing of the difference at high overpotentials further corroborate the idea that Imanishi's experiments encounter a sheet resistance effect.

Implications.— The favorable comparisons between the behavior of the model and the experimental systems suggest that these thin-film experiments are encountering sheet resistance at overpotentials common to operating fuel cells. Although it is difficult at this point to provide quantitative guidance, it should be pointed out that in experiments where the thickness of the LSM electrode falls below 1 μm, there may be sheet resistance to contend with. This is the case for patterned electrodes, thin films, or porous electrodes. Especially in the case of nanostructuring, it would seem prudent to take current collection into account when designing new electrode architectures.

Conclusion

A model of the cathodic reaction on thin-film MIECs and a comparison with experimental data suggests that sheet resistance can play an important role in the overall cell resistance, becoming more important as polarization increases. A model incorporating the phenomenon was derived, and its finite volume-based numerical solution was stable in two dimensions at most practical overpotentials. Simulations using parameters collected from the literature show an ionic transport limitation at low overpotentials, and sheet resistance at high overpotentials. Comparisons with experimental studies revealed that the model is much more resistive, but the difference is much smaller when compared against a study on epitaxial and near-epitaxial films. The general two-regime linear shape of the I-V curves generated by the model seems to match most of those measured experimentally. The major implication is that current collection must be considered in the design of LSM electrodes, especially as length scales decrease.

Acknowledgments

This work was supported by the U.S. DOE University Coal Program under grant no. DE-FG26-06NT42735, DOE Basic Energy Science under grant no. DE-FG02-06ER15837, and NSF under grant no. 0511815. Additional support for David Mebane was provided through a Boeing Fellowship.

Georgia Institute of Technology assisted in meeting the publication costs of this article.

References

1. F. S. Baumann, J. Fleig, H. U. Habermeier, and J. Maier, *Solid State Ionics*, **177**, 1071 (2006).
2. V. Brichzin, J. Fleig, H. U. Habermeier, G. Cristiani, and J. Maier, *Solid State Ionics*, **152**, 499 (2002).
3. V. Brichzin, J. Fleig, H. U. Habermeier, and J. Maier, *Electrochem. Solid-State Lett.*, **3**, 403 (2000).
4. A. Endo, H. Fukunaga, C. Wen, and K. Yamada, *Solid State Ionics*, **135**, 353 (2000).
5. A. Endo, S. Wada, C. J. Wen, H. Komiyama, and K. Yamada, *J. Electrochem. Soc.*, **145**, L35 (1998).
6. A. Endo, M. Ihara, H. Komiyama, and K. Yamada, *Solid State Ionics*, **86-8**, 1191 (1996).
7. N. Imanishi, T. Matsumura, Y. Sumiya, K. Yoshimura, A. Hirano, Y. Takeda, D. Mori, and R. Kanno, *Solid State Ionics*, **174**, 245 (2004).
8. T. Ioroi, T. Hara, Y. Uchimoto, Z. Ogumi, and Z. Takehara, *J. Electrochem. Soc.*, **144**, 1362 (1997).
9. T. Ioroi, T. Hara, Y. Uchimoto, Z. Ogumi, and Z. Takehara, *J. Electrochem. Soc.*, **145**, 1999 (1998).
10. T. Kawada, J. Suzuki, M. Sase, A. Kaimai, K. Yashiro, Y. Nigara, J. Mizusaki, K. Kawamura, and H. Yugami, *J. Electrochem. Soc.*, **149**, E252 (2002).
11. T. Kawada, K. Masuda, J. Suzuki, A. Kaimai, K. Kawamura, Y. Nigara, J. Mizusaki, H. Yugami, H. Arashi, N. Sakai, and H. Yokokawa, *Solid State Ionics*, **121**, 271 (1999).
12. E. Koep, C. Compson, M. L. Liu, and Z. P. Zhou, *Solid State Ionics*, **176**, 1 (2005).
13. E. Koep, D. S. Mebane, R. Das, C. Compson, and M. L. Liu, *Electrochem. Solid-State Lett.*, **8**, A592 (2005).
14. C. A. Mims, N. I. Joos, P. A. W. van der Heide, A. J. Jacobson, C. Chen, C. W. Chu, B. I. Kim, and S. S. Perry, *Electrochem. Solid-State Lett.*, **3**, 59 (2000).
15. J. Mizusaki, T. Saito, and H. Tagawa, *J. Electrochem. Soc.*, **143**, 3065 (1996).
16. D. Mori, H. Oka, Y. Suzuki, N. Sonoyama, A. Yamada, R. Kanno, Y. Sumiya, N. Imanishi, and Y. Takeda, *Solid State Ionics*, **177**, 535 (2006).
17. A. Ringuede and J. Fouletier, *Solid State Ionics*, **139**, 167 (2001).
18. Y. Takeda, R. Kanno, M. Noda, Y. Tomida, and O. Yamamoto, *J. Electrochem. Soc.*, **134**, 2656 (1987).
19. Y. L. Yang, C. L. Chen, S. Y. Chen, C. W. Chu, and A. J. Jacobson, *J. Electrochem. Soc.*, **147**, 4001 (2000).
20. Y. M. L. Yang, A. J. Jacobson, C. L. Chen, G. P. Luo, K. D. Ross, and C. W. Chu, *Appl. Phys. Lett.*, **79**, 776 (2001).
21. T. R. Brumleve and R. P. Buck, *J. Electroanal. Chem. Interfacial Electrochem.*, **90**, 1 (1978).
22. T. R. Brumleve and R. P. Buck, *J. Electroanal. Chem. Interfacial Electrochem.*, **126**, 73 (1981).
23. J. Jamnik and J. Maier, *Phys. Chem. Chem. Phys.*, **3**, 1668 (2001).
24. S. B. Adler, J. A. Lane, and B. C. H. Steele, *J. Electrochem. Soc.*, **143**, 3554 (1996).
25. A. M. Svensson, S. Sunde, and K. Nisancioglu, *J. Electrochem. Soc.*, **144**, 2719 (1997).
26. A. M. Svensson, S. Sunde, and K. Nisancioglu, *J. Electrochem. Soc.*, **145**, 1390 (1998).
27. J. Fleig, *J. Power Sources*, **105**, 228 (2002).
28. J. Fleig and J. Maier, *J. Eur. Ceram. Soc.*, **24**, 1343 (2004).
29. G. W. Coffey, L. R. Pederson, and P. C. Rieke, *J. Electrochem. Soc.*, **150**, A1139 (2003).
30. R. E. Williford and P. Singh, *J. Power Sources*, **128**, 45 (2004).
31. J. Deseure, Y. Bultel, L. Dessemond, and E. Siebert, *Solid State Ionics*, **176**, 235 (2005).
32. W. G. Wang, Y. L. Liu, R. Barfod, S. B. Schougaard, P. Gordes, S. Ramousse, P. V. Hendriksen, and M. Mogensen, *Electrochem. Solid-State Lett.*, **8**, A619 (2005).
33. A. Princivalle, D. Perednis, R. Neagu, and E. Djurado, *Chem. Mater.*, **16**, 3733 (2004).
34. M. Mamak, G. S. Metraux, S. Petrov, N. Coombs, G. A. Ozin, and M. A. Green, *J. Am. Chem. Soc.*, **125**, 5161 (2003).
35. R. W. Evitts, Ph.D. Thesis, University of Sasketchewan, Saskatoon, Sasketchewan, Canada (1997).
36. D. S. Mebane and M. L. Liu, *J. Solid State Electrochem.*, **10**, 575 (2006).
37. J. Fleig, *Phys. Chem. Chem. Phys.*, **7**, 2027 (2005).
38. J. Newman and K. E. Thomas-Alyea, *Electrochemical Systems*, 3rd ed., Wiley-Interscience, Hoboken, NJ (2004).
39. S. Patankar, *Numerical Heat Transfer and Fluid Flow*, Hemisphere Publishing, New York (1980).
40. J. H. Kuo, H. U. Anderson, and D. M. Sparlin, *J. Solid State Chem.*, **83**, 52 (1989).
41. B. A. vanHassel, T. Kawada, N. Sakai, H. Yokokawa, M. Dokiya, and H. J. M. Bouwmeester, *Solid State Ionics*, **66**, 295 (1993).
42. J. Nowotny and M. Rekas, *J. Am. Ceram. Soc.*, **81**, 67 (1998).
43. J. Mizusaki, N. Mori, H. Takai, Y. Yonemura, H. Minamiue, H. Tagawa, M. Dokiya, H. Inaba, K. Naraya, T. Sasamoto, and T. Hashimoto, *Solid State Ionics*, **129**, 163 (2000).
44. F. W. Poulsen, *Solid State Ionics*, **129**, 145 (2000).
45. A. N. Grundy, B. Hallstedt, and L. J. Gauckler, *CALPHAD: Comput. Coupling Phase Diagrams Thermochem.*, **28**, 191 (2004).
46. J. A. Kilner, R. A. DeSouza, and I. C. Fullarton, *Solid State Ionics*, **86-8**, 703 (1996).
47. R. A. De Souza and J. A. Kilner, *Solid State Ionics*, **126**, 153 (1999).
48. R. A. De Souza and J. A. Kilner, *Solid State Ionics*, **106**, 175 (1998).
49. N. Q. Minh and T. Takahashi, *Science and Technology of Ceramic Fuel Cells*, Elsevier Science, New York (1995).
50. I. Riess, *Mater. Sci. Eng., B*, **12**, 351 (1992).